Kwiatek, G., Goebel, T., Dresen, G. (2014): Seismic moment tensor and b-value variations over successive seismic cycles in laboratory stick-slip experiments. - *Geophysical Research Letters*, *41*, 16, p. 5838-5846

DOI: http://doi.org/10.1002/2014GL060159

AGU PUBLICATIONS

Geophysical Research Letters

RESEARCH LETTER
10.1002/2014GL060159

Key Points:
- Stick slips analyzed using moment tensor inversion of acoustic emissions
- Stick-slip sliding processes are clearly controlled by the initial fault state
- Changes in b values attributed to the variations in micromechanical processes

Supporting Information:
- Readme
- Figure S1
- Figure S2
- Figure S3
- Figure S4
- Figure S5
- Figure S6
- Figure S7

Correspondence to:
G. Kwiatek,
kwiatek@gfz-potsdam.de

Citation:
Kwiatek, G., T. H. W. Goebel, and G. Dresen (2014), Seismic moment tensor and *b* value variations over successive seismic cycles in laboratory stick-slip experiments, *Geophys. Res. Lett.*, *41*, 5838–5846, doi:10.1002/2014GL060159.

Received 14 JUL 2014
Accepted 3 AUG 2014
Accepted article online 7 AUG 2014
Published online 20 AUG 2014

Seismic moment tensor and *b* value variations over successive seismic cycles in laboratory stick-slip experiments

Grzegorz Kwiatek[1], T. H. W. Goebel[2], and Georg Dresen[1]

[1]Section 3.2: Geomechanics and Rheology, Helmholtz Centre Potsdam, GFZ German Research Centre for Geosciences, Potsdam, Germany, [2]California Institute of Technology, Seismological Laboratory, Pasadena, California, USA

Abstract The formation of fault damage due to slip under high normal stresses can rarely be monitored under in situ conditions. To advance our understanding of microfracture processes, we investigated stick-slip events on Westerly granite samples containing the following: (1) a planar saw cut fault and (2) a fault developed from a fresh fracture surface. We examined temporal changes of seismic moment tensors and *b* values of acoustic emission (AE) events. During experiment on the saw cut surface, small AEs exhibiting non-double-couple components were observed continuously and strong AEs displaying double-couple components were visible only when approaching the slip onsets. Sliding on naturally fractured surfaces showed, in addition to double-couple components, significant volumetric contributions, especially during the interslip periods and immediately after stick-slip events indicating substantial shear-enhanced compaction within a relatively broad damage zone. The obtained results shed light on how differences in fault structure control the kinematics of microseismicity during different periods of the seismic cycle.

1. Introduction

Nearly 50 years have passed since the seminal work of *Brace and Byerlee* [1966] who first suggested that the stick-slip events frequently accompanying frictional sliding in laboratory experiments may be regarded as an experimental analog of shallow earthquakes. Since then, numerous experimental studies have investigated physical processes and characteristics of frictional sliding, extending the link between microseismicity in the laboratory and nature [e.g., *Goebel et al.*, 2013a, 2014a; *Thompson et al.*, 2009]. Extrapolating these laboratory observations to the field scale may provide important insights into the physics governing source processes of earthquakes [*McGarr and Fletcher*, 2003; *McGarr*, 2012].

The analysis of acoustic emissions (AE) monitored during rock fracture and friction tests allow description of the spatiotemporal evolution of damage [*Stanchits et al.*, 2011]. The AE source characterization provides insight into the micromechanical processes such as initiation and coalescence of cracks in rock samples [*Lockner*, 1993; *Graham et al.*, 2010], fracture nucleation, formation of the fracture surface [*Sellers et al.*, 2003], unstable sample failure, and subsequent shear sliding along the generated fault surfaces. Simple techniques have been developed to assess AE faulting mechanisms using first motions of *P* waves [e.g., *Zang et al.*, 1998]. However, more elaborated methods involve calculations of the full moment tensor (MT) using seismic waveform data [e.g., *Ohtsu*, 2000; *Graham et al.*, 2010; *Davi et al.*, 2013; *Kwiatek et al.*, 2014].

Inverting seismic data to determine the full MT helps to constrain fault plane parameters as well as the amount of volumetric and nonvolumetric strain in the seismic source [*Knopoff and Randall*, 1970]. The decomposition of MTs into volumetric and deviatoric components is a useful tool for the understanding of physical processes occurring during natural and induced earthquakes [e.g., *Gibowicz et al.*, 1991; *Ross et al.*, 1996; *Collins et al.*, 2002; *Fischer and Guest*, 2011]. The MT inversion can be applied to AEs recorded in laboratory experiments performed at well-constrained boundary conditions. The interpretation of source kinematics at the microscale may then be related to field observations and earthquake source parameters observed in situ [*McGarr and Fletcher*, 2003; *McGarr et al.*, 2010; *McLaskey and Glaser*, 2011; *McGarr*, 2012]. Analysis of AE source mechanisms may shed light on the physics of earthquakes, for example, rupture dynamics, fault complexity, the role of pore pressure in seismogenic processes [*Fischer and Guest*, 2011], and damage-related radiation of seismic energy [*Ben-Zion and Ampuero*, 2009; *Castro and Ben-Zion*, 2013].

The MT inversion technique has already been applied in the analysis of AE activity in underground laboratories [*Manthei et al.*, 2001; *Collins et al.*, 2002; *Manthei*, 2005] as well as in laboratory experiments on rock samples [*Ohtsu*, 2000; *Sellers et al.*, 2003; *Thompson et al.*, 2009; *Graham et al.*, 2010; *Davi et al.*, 2013]. However, full moment tensor inversion (FMTI) of laboratory data is sensitive to data quality, errors in polarities, and the determination of phase onsets in noisy environments. Site effects such as sensor coupling and sensor characteristics affect the results of FMTI of AEs (see *Sellers et al.* [2003] for a comprehensive review). Various (relative) calibration techniques have been developed for AE experiments performed in confining chamber at elevated pressures [e.g., *Sellers et al.*, 2003; *Davi et al.*, 2013; *Kwiatek et al.*, 2014].

Here we performed a detailed analysis of the AE-derived MTs recorded during a series of stick-slip events in laboratory experiments on two Westerly Granite samples. The selected samples exhibited different fault roughness (saw cut and naturally fractured surface) in order to investigate the interplay between roughness and microfracture processes during slip, contributing to the previous results of *Goebel et al.* [2013a], who suggested that naturally fractured surface resembled natural fault structures more closely. The temporal changes of MT parameters calculated from AE activity are investigated and compared to variations in the slopes of the corresponding frequency-magnitude distributions (*b* values) and the differential stress.

2. Experimental Setup

The triaxial stick-slip tests were conducted on two cylindrical samples of Westerly Granite with dimensions of 40×107 mm and 50×102 mm, respectively, deformed at constant strain rate [cf. *Goebel et al.*, 2013b] $3 \times 10^{-6}\,s^{-1}$. The experiments were performed on oven-dried samples at room temperature on specimens encapsulated by a rubber sleeve to prevent the intrusion of the confining oil. The first sample, $S1_{frac}$, was prepared with a 2.5 cm deep notch inclined at 30° to the cylinder axis. This specimen was first fractured at 75 MPa confining pressure producing a rough fault surface. The following stick-slip experiment was performed at constant confining pressure at $P_C = 150$ MPa. A second sample, $S2_{cut}$, was prepared with a smooth saw cut across the entire sample at 30° to the cylinder axis. The sample surface was prepared using a #60 silicon carbide powder with grain sizes between 212 and 300 μm. The sample was then loaded at a confining pressure of 133 MPa until episodic stick-slip failure occurred. During both experiments we measured vertical strain using a pair of strain gauges glued directly on the sample above and below the fault. Due to the experimental setup, no radial strain data could be measured within the fault zone.

AE activity was recorded by 16 AE sensors (resonant frequency 1 MHz, typical frequency content 0.3–0.8 MHz) glued directly to the surface of the specimen securing an almost complete azimuthal coverage of AE events. Event waveforms were recorded in triggered mode at 10 MHz sampling frequency and 16 bit amplitude resolution. Throughout the experiment, a series of *P* wave velocity measurements was performed using ultrasonic transmission (UT) that provided a time-dependent anisotropic velocity model composed of five equally spaced horizontal layers and one vertical layer. The velocity model was updated every 30 s throughout the experiment and used to determine hypocenter locations taking into account differences between vertical and horizontal velocities resulting in typical location accuracy ±2 mm [*Stanchits et al.*, 2006]. UT and AE waveforms were automatically discriminated using offline waveform processing software [*Stanchits et al.*, 2006]. The high signal-to-noise ratio of typically exceeding 30 dB allowed to easily pick *P* wave onset times and first *P* wave amplitudes using automatic picking algorithm based on the Akaike information criterion. The first *P* wave amplitudes were corrected for coupling quality of AE sensors and incidence angle using the ultrasonic calibration technique [*Kwiatek et al.*, 2014] before performing FMTI. The AE magnitude was calculated using $M_{AE} = \log_{10}\left(\frac{1}{n}\sum_{i=1}^{n}(A_i R_i)^2\right)^{0.5}$, where A_i and R_i are the first *P* wave amplitude and source-receiver distance for sensor *i*, respectively. This magnitude reveals relative size differences between AE events and is not directly calibrated to the physical size of the events.

3. Data and Method

A total number of 97,847 AE events were located during experiment $S1_{frac}$. For 42,003 AE events a FMTI using available 12 first *P* wave amplitudes was performed. In contrast, the total seismic activity in the experiment $S2_{cut}$ was nearly 100 times lower (Figures 1a and 1b) resulting in a successful determination of 1046 MTs based on 10 or more first motion amplitudes. The choice of lower minimum number of *P* wave motions in case of experiment $S2_{cut}$ did not increase the RMS errors of MTs in comparison to those

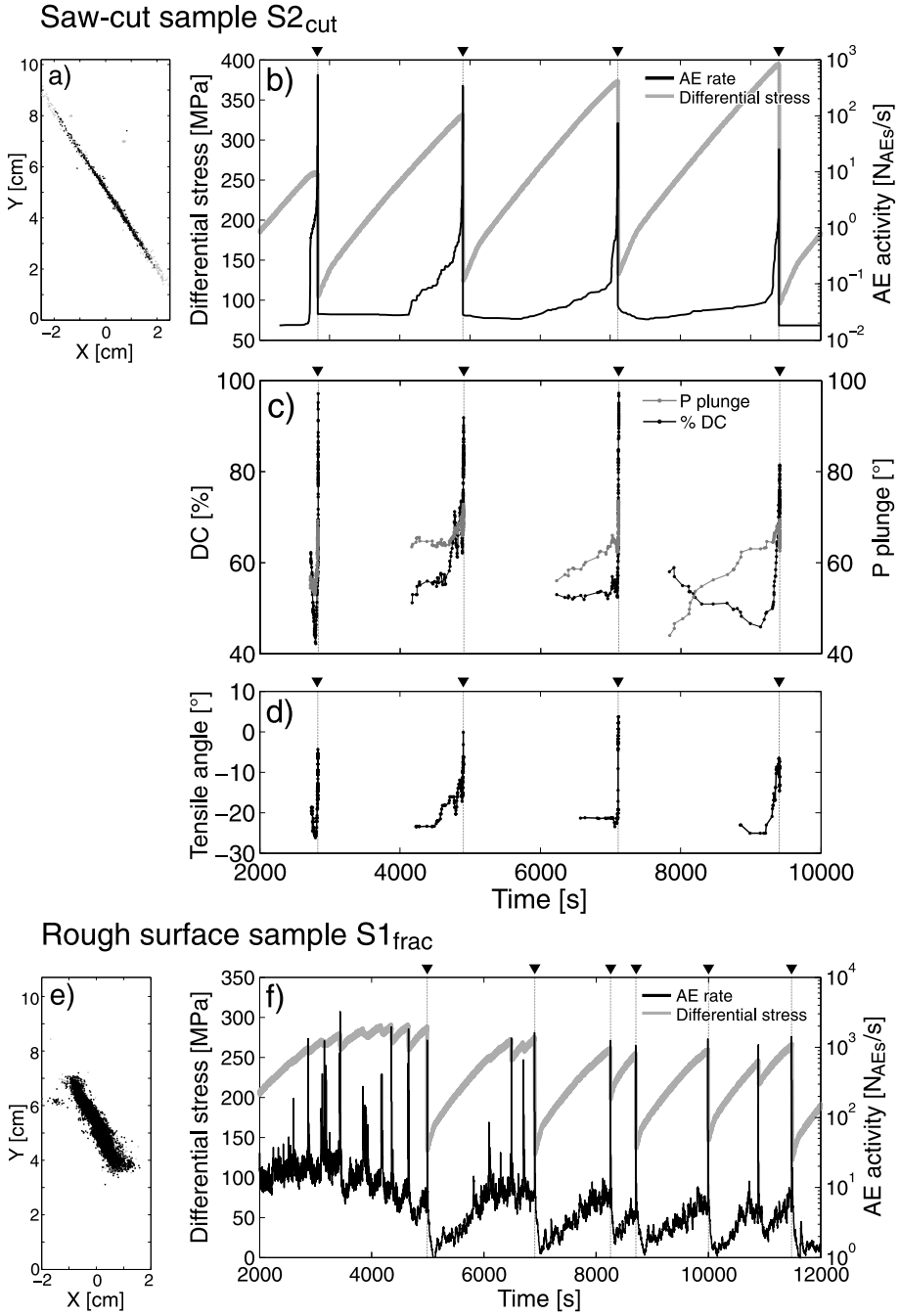

Figure 1. (a) Spatial distribution of AE activity for $S2_{cut}$ experiment. Hypocenters that did not meet the quality criteria for FMTI are plotted in the background in gray. (b–d) Temporal changes in differential stress, AE rate, and MT-derived characteristics for $S2_{cut}$ experiment. The onsets of investigated slips are marked with inverted triangles (cf. Figures 2a–2c). Dots show places at which moving averages were calculated. Temporal changes in percentage of DC component, tensile angle, and plunge of *P* axis while approaching the slip indicate an increase in shearing over saw cut surface in addition to persistent compaction of the material forming the fault zone. (e) Spatial distribution of AE activity for $S1_{frac}$ experiment; (f) temporal changes in AE rate and differential stress (cf. Figures 2d–2f).

calculated for $S1_{frac}$. The FMTI was performed using software designed for the analysis of mining-induced seismicity based on the formal description presented in *Wiejacz* [1992]. The resulting MTs were decomposed into isotropic (ISO), compensated linear vector dipole (CLVD), and double-couple (DC) components following *Knopoff and Randall* [1970] with ISO, CLVD, and DC percentages calculated according to *Vavryčuk*

[2001]. The ISO components reflect the volumetric change in seismic sources, whereas CLVD and DC represent the deviatoric parts of calculated MTs. An increase in negative ISO suggests more implosive character of the seismic source, whereas positive ISO components display explosive character of the source. Using ISO and CLVD components, we additionally calculated the "tensile" angle α, which is the angle between the slip vector and its projection on the fault surface [*Vavryčuk*, 2001; *Kwiatek and Ben-Zion*, 2013]. The coherent changes in ISO and CLVD components are reflected in tensile angle change that corresponds to the shear-enhanced compaction or extension with the shear component in the seismic source, depending on signs of ISO and CLVD components. For $\alpha < 0°$ (ISO < 0 and CLVD < 0), shear-enhanced compaction is assumed, $\alpha = 0°$ corresponds to no volumetric change (= pure shearing), and extension with shearing component is assumed for $\alpha > 0°$ (ISO > 0 and CLVD > 0, see Figure S1 in the supporting information). From the deviatoric part of the MTs, we extracted the *P* axis plunges. A *P* plunge equal to $\delta_P = 90°$ and $\delta_P = 0°$ corresponds to the direction aligned with the direction of maximum compression and direction perpendicular to it.

Due to the large AE activity rate, we investigated temporal variations in the AE activity, MT-derived parameters (ISO, CLVD, DC contributions, *P* plunge, and tensile angle) at different periods of the seismic cycle using a sliding window containing 50 events. Except for the AE activity, the remaining MT-derived characteristics were calculated in a way to not mix AEs from following stick-slip episodes. For the *b* value estimates during experiment $S1_{frac}$, we increased the window size to 200 events based on stability tests with a range of window sizes [cf. *Goebel et al.*, 2013b]. For the saw cut surface sample, the activity was too low to calculate *b* value changes within sliding time windows. Instead, we defined two time intervals, i.e., an interslip phase (time between slip and 30 s before the following slip) and a preslip phase (30 s before slip to slip onset), which were used to calculate the frequency-magnitude characteristics. For the discussion of experiment $S1_{frac}$, we also defined a postslip period, i.e., a period of 10 s after slip onset that showed a power law activity decay [*Goebel et al.*, 2013a]. The acquisition system does not allow for investigating the AE source characteristics during slip ($<$0.2 ms) due to strong disturbances in noise conditions originating from macroscopic slip.

4. Results

4.1. AE Rate and Differential Stress

Stick-slip events on the saw cut surface were associated with large stress drops ranging between 150 and 300 MPa. The connected AE activity occurred at or in the vicinity of the slip plane (Figure 1a). The cumulative slip on this plane resulted in the creation of a thin ($<$2 mm) gouge layer likely related to the fracture of fault asperities (see Figure S2 in the supporting information). The AE activity was low during the interslip phases ($<$1 AE/20 s), increased rapidly in the preslip phase (Figure 1b), and ceased immediately after the slip so that no AE aftershocks were observed.

Frictional sliding along the natural fracture surface in experiment $S1_{frac}$ resulted in a series of small and large slip events and a wider damage zone ($<$15 mm) with a broad AE distribution across the fault (Figures 1e and 1f) [*Goebel et al.*, 2014b]. The AE activity in interslip phases was higher (~5 AEs/s) in comparison to the saw cut sample and increased slowly in preslip phases. The peak in AE rates ($>$1000 AEs/s) was reached immediately after the slip events and showed a characteristic aftershock-like decrease over 8–20 s. For experiment $S1_{frac}$, we focused on the periods of strongest variations in MT components and derived MT parameters 50 s before until 50 s after fault slip and large stress drops (Figure 1f). Low stress drops did not produce significant changes in MT-derived parameters.

4.2. Temporal Changes in MT-Derived Parameters

The deformation along the saw cut surface resulted in approximately 90% of fault-parallel AE events with dip direction in accordance to the macroscopic slip (cf. Figure S3 in the supporting information). On smaller timescales, we observed changes in MT-derived parameters both within a stick-slip (seismic) cycle and slight changes with successive stick-slip cycles (Figures 1c and 1d). Interslip phases displayed relatively low contributions of DC components and lower values of *P* axis plunge (Figures 1c and 2a). This is accompanied by negative non-DC components as well as negative tensile angles (Figures 1d and 2b). The macroscopic vertical strain data present sample shortening in this phase. However, in the preslip phase, a rapid increase in the average amount of DC components at the expense of non-DC components is observed, accompanied by

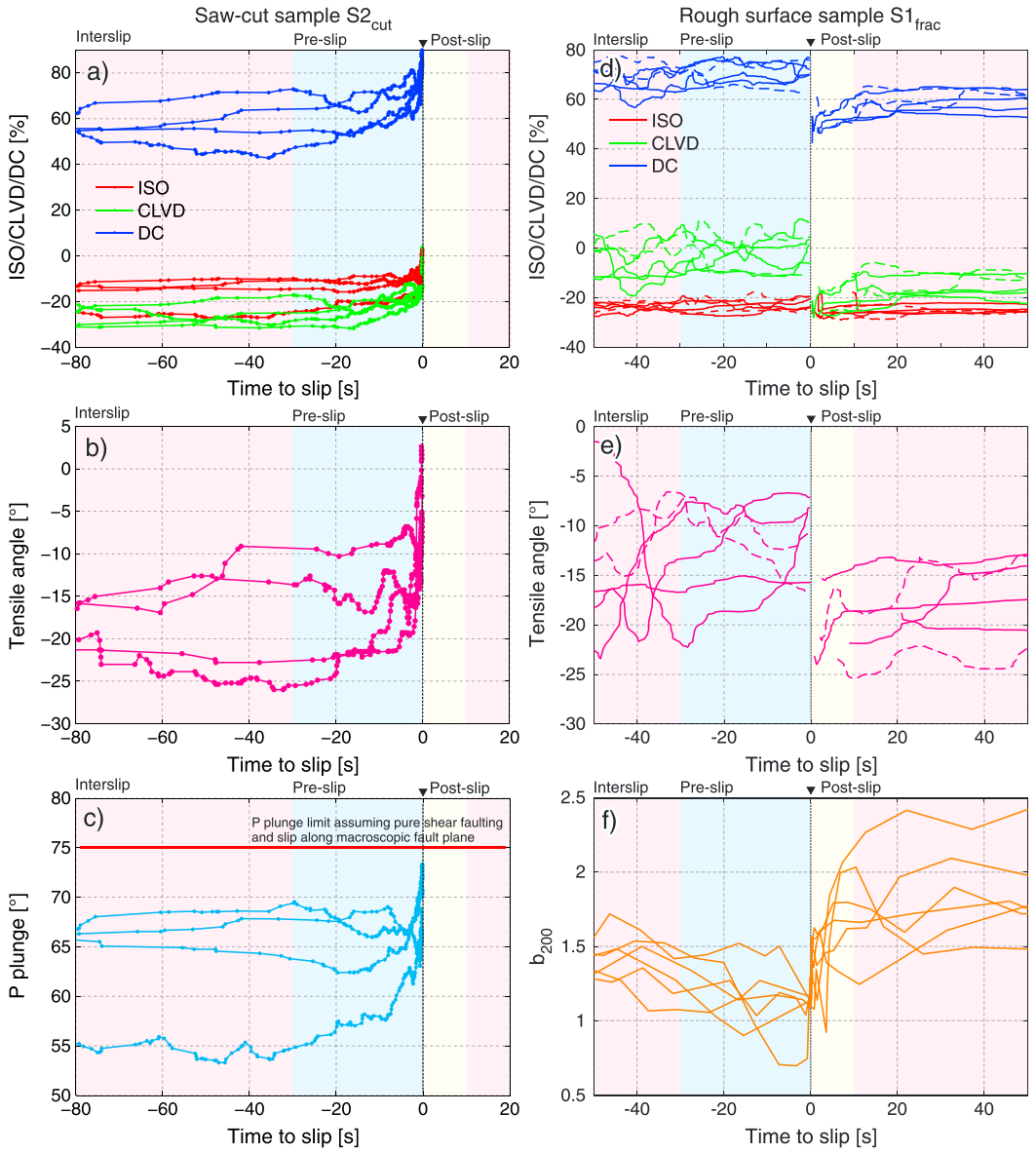

Figure 2. Changes in MT-derived parameters and *b* values before and after slip events for (a–c) experiment $S2_{cut}$ and (d–f) experiment $S1_{frac}$. Time $t = 0$ s corresponds to the slip onset and is marked with inverted triangle. Dots show places at which moving averages were calculated (Figures 2a–2c).

a change in macroscopic vertical deformation rates. The tensile angles typically show an abrupt increase of >15–20° (Figure 2b) as well as a systematic rotation of average *P* axis plunges toward higher values in comparison to interslip phases (Figure 2c). In addition, a slow increase in the tensile angle is visible as well as the *P* plunge in consecutive preslip periods (excluding the fourth slip), accompanied by the decrease in peak AE rates.

In the following, we compared all interslip and preslip periods with respect to differences in frequency-magnitude distributions (FMDs) of AEs and differences in changes of MT characteristics with AE magnitude. Figure 3a presents a comparison of FMDs calculated from all AEs that occurred during interslip and preslip periods. The interslip periods exhibited predominantly low AE magnitudes with FMDs that can be described by a power law. In contrast, the FMDs of AEs from preslip periods display a non-self-similar, bimodal shape with a prominent peak at higher AE magnitudes. We also notice that larger AEs contain less ISO components, whereas small events contain more ISO components (Figure 3b).

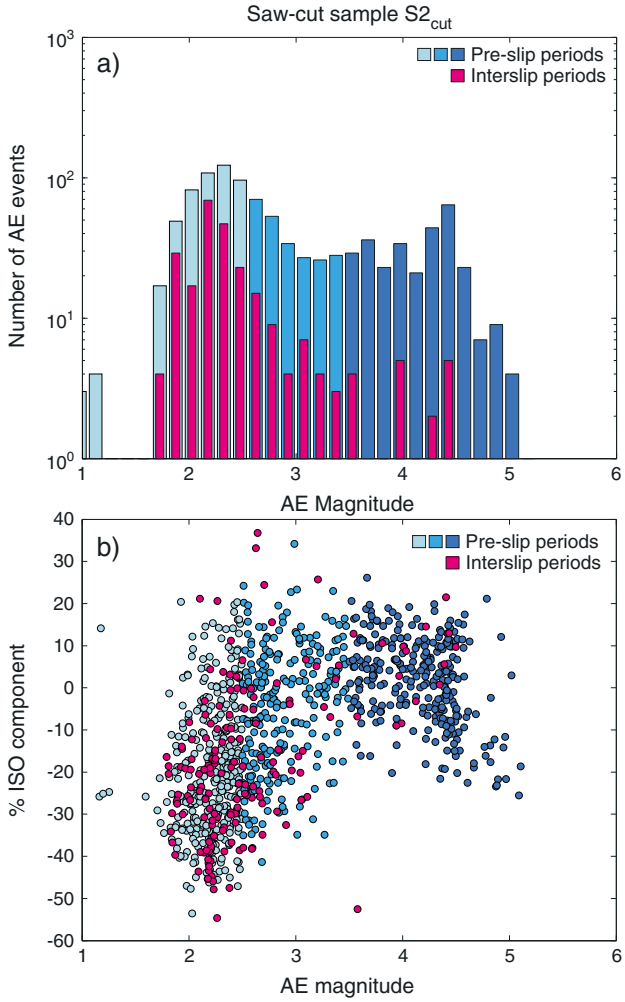

Figure 3. (a) Comparison of FMDs computed for AEs occurring during preslip and interslip periods of experiment $S2_{cut}$. (b) Relationship between AE magnitude and the amount of ISO component for AEs from preslip and interslip periods. Note that the AE magnitude is specific to the here employed transducers and is not calibrated in an absolute sense.

Successive stick-slip events along the rough surface in experiment $S1_{frac}$ resulted in rapid temporal changes in MT components in response to high differential stress drops. We selected five stick-slip episodes connected to significant macroscopic stress drop ($\Delta\sigma > 50$ MPa) and investigated temporal changes in MT-derived characteristics as well as *b* values (Figures 2d–2f). From about 40 s prior to slip onset we observed a decrease in *b* values (Figure 2f) followed by a rapid, postfailure increase. The amount of *b* value increase after slip is inversely correlated with the stress drop magnitude [*Goebel et al.*, 2013b]. The ISO components remain constant during the stick-slip cycle at about ISO = −20% suggesting small, but persistent compaction (Figure 2d). After fault slip, the changes in CLVD and DC components, as well as the tensile angle (Figure 2e), are generally the opposite of what was observed during slip events on the saw cut surface. During the postslip phase the CLVD and DC components, as well as tensile angle, show a significant decrease with subsequent fast recovery in the early parts of the following interslip phase. Similar to the saw cut sample we compared FMDs and AE magnitude dependence of MT-derived characteristics between preslip and postslip periods (Figures S4 and S5 in the supporting information). We find that FMDs created from all preslip and postslip periods do not express any signature of deviation from the power law behavior. Also, relations between MT-derived characteristics and AE magnitudes are very similar for AEs preceding and following the slip episodes.

5. Discussion

Our study was motivated by a comparison between a simple, relatively smooth fault represented by a saw cut surface, and a fault that evolves from an incipient fracture, which mimics parts of the expected fault complexity in nature. Fault complexity and structural heterogeneity resulted in different macroscopic mechanical behavior and microscopic deformation inferred from AE events. The macroscopic strain data provide point measurements of the axial strain component above and below the fault, as radial strain gauges could not be installed inside the fault zone. Consequently our information on macroscopic bulk volumetric changes in the sample (especially in the fault zone) is quite limited. On the other hand, the AE-derived MTs can provide relative microscopic volumetric strain information via, e.g., Kostrov's strain formula, as AE sensors are not calibrated in an absolute sense. In addition, the AE-derived strain represents only a small fraction of the total crack damage, likely <5% [*Zang et al.*, 1998].

Nevertheless, the micromechanical processes observed in AE-derived MTs in both experiments are in agreement with the macroscopic vertical strain data as well as with the stress state of the respective faults.

Each slip event is associated with systematic changes of all MT-derived parameters as well as *b* values or characteristics of FMDs. Interestingly, these temporal changes are recurrent with slip events but differ in many aspects for the two tests with different fault topography (cf. Figures 2a–2c and 2d–2f).

As example, in interslip periods of experiment $S2_{cut}$, the vertical macroscopic shortening of the sample is observed in strain data. This is associated with the existence of small AEs displaying microscopic compaction (cf. Figure 3). This observation suggests that the voids existing due to the remaining roughness of the saw cut surface are progressively closed in a shear-enhanced compaction manner at relatively low values of normal stress. However, in preslip periods, large AEs with high contribution of DC components in their source mechanisms become abundant (sometimes displaying in addition positive ISO components). These AE events constitute additional physical process that is overlapping with the process of persistent compaction (still expressed in low-magnitude AEs, however, now more abundant) leading to bimodal FMD. Macroscopically, this period is reflected in changes (typically decrease) of the vertical deformation rate before slip which deviate from purely linear (elastic) deformation observed in interslip periods. This suggests the preslip period is characterized by increase in a microscale shear sliding, sometimes with slight dilation component, being overall a signature of the approaching large slip. These microshear slidings seem to generate a transient change in the roughness of the sample that would explain the concurrent increase in the low-magnitude AE activity persistently displaying shear-enhanced compaction behavior.

In addition, some signatures of fault evolution are visible during experiment $S2_{cut}$. The subsequent slip phases on the saw cut surface tend to decrease the peak AE rates as well as the relative number of AEs displaying non-DC components during following stick-slip cycles (Figures 2b–2d). This might indicate that damage, for example, due to grain comminution and asperity fracturing was predominantly created during initial stick slips. Consequently, the fault may seem to evolve into some steady state roughness during which most of the elastic energy is released during macroscopic slip on the fault.

Another interesting feature observed in the experiment $S2_{cut}$ is the correlation between *P* axis plunge and the change in non-DC components, a feature that is not easily explainable using classical MT theory. However, the correlation may be easily interpreted using the shear-tensile source model (Figure S6 in the supporting information). Assuming the AEs displaying pure DC source mechanism without any non-DC component and having one nodal plane parallel to the macroscopic fault surface dipping 60° (Figure S6a in the supporting information), a *P* plunge of 75° is expected. However, the tensile angle will be nonzero in the presence of any non-DC components. This will also result in *P* axis rotation toward lower plunge angles for shear-enhanced compaction (Figure S6b in the supporting information) or toward higher plunge angles for extension with shear component. Therefore, the observation of *P* plunge rotation in experiment $S2_{cut}$ also indicates episodic compaction or dilation during shear.

Overall, it is conceivable that in the interslip phase the increasing normal stress reduces the remaining roughness of the sample resulting in small AE events displaying shear-enhanced compaction, a concomitant decrease in tensile angle and rotation of the *P* axes toward the fault normal (decreasing plunge of *P*) in approaching the next slip event. In preslip phases, shear-enhanced compaction expressed as small AEs continues (Figure 3) at higher AE rate. In addition, the macroscopic slip event preparation is accompanied by a series of microslips expressed in large magnitude AEs displaying shearing behavior. Finally, the following slip phases suggest progressive removal of fault roughness, as expressed in decreasing AE activity and increase in the tensile angle.

Sliding along the rough surface instead results in certain level of compaction observed in interslip phases and expressed in negative ISO components of MTs and supported by strain data. The onset of the macroscopic slip is signaled by *b* values decrease in preslip phase and shows a rapid postslip recovery (Figure 2f). No significant changes in MT mechanisms with AE magnitudes between preslip and postslip phases were found (Figures S4 and S5 in the supporting information). However, the postslip phase is characterized by an abrupt reduction of AE DC and CLVD components as also indicated by increasing negative tensile angles (Figures 2d and 2e). The observed changes in the MT characteristics between preslip and postslip phase can be interpreted as a transition from minor compaction to pronounced (due to concurrent increase in AE activity) shear-enhanced compaction of fault gouge lasting a couple of seconds following a slip episode. Progressive sliding along the fault with pronounced topography after a rupture event likely involves some dilation/compaction of the fault zone and shearing along the anastomosing and localized slip bands within the fault damage zone [*Thompson et al.*, 2009; *Goebel et al.*, 2012] (cf. Figure S7 in the supporting information). We posit that the postslip increase

of *b* values between individual slip events is related to intensive grain crushing and compaction of gouge material populating the fault zones. The overall higher AE activity in $S1_{frac}$ experiment in comparison to $S2_{cut}$ despite of differences in stress drops is related to the broader damage zone of the rough surface sample.

6. Summary and Conclusions

Recent studies of continuously monitored AE activity during stick-slip experiments have provided new insights in the micromechanics of rupture nucleation and asperity failure along fracture surfaces in rock samples and rock-analog materials [*Goebel et al.*, 2012; *McLaskey and Glaser*, 2012; *McLaskey and Kilgore*, 2013]. In this study, we extend these results by analyzing the micromechanics of deformation within simple and complex fault zones under upper crustal stress conditions and by investigating temporal changes in MT-derived parameters, as well as *b* values of AE events.

We found that the observed MT components of AEs and the sliding processes are clearly controlled by the initial fault state. Loading of a saw cut sample resulted in continuous shear-enhanced compaction as expressed by the non-DC components of small AEs overlapping with many stronger AEs with predominantly DC components occurring just before a macroscopic slip. Likewise, sliding along a rough surface produced AEs displaying significant negative non-DC components. However, in contrast to the saw cut sample $S2_{cut}$ shear-enhanced compaction of comminuted material in the fault zone significantly increased after stress drop.

Observations of significant non-DC components in mature fault zones are quite rare [*Stierle et al.*, 2014b]. This may originate from the fact that non-DC processes may be hidden due to lower magnitudes of non-DC events, as observed in both experiments, and/or insufficient sensitivity of monitoring networks. Non-DC components may also be obstructed during the rupture process by dominating shear slip along the fault [*Stierle et al.*, 2014a] or in some cases simply discountable due to prolonged and repeating slips removing the fault roughness that could be capable to produce significant non-DC events, as demonstrated in the saw cut sample. Thus, upscaling of our experimental findings to seismological observations from larger faults is not trivial. In general, brittle damage produced during earthquake ruptures is expected to produce at least some tensile component [*Ben-Zion and Ampuero*, 2009], in particular, since complex fault surface structures are typically observed in fault zones [e.g., *Ben-Zion and Sammis*, 2003; *Brodsky et al.*, 2011; *Savage and Brodsky*, 2011]. This would suggest that results from rough surface samples with complex fault geometry better represent fault zone deformation (cf. Figure S7) [*Thompson et al.*, 2009].

The observed rotations of *P* axes of MTs due to increasing non-DC components may have implications for reliability of the stress inversion from focal mechanisms. Stress inversion routines assume input data displaying pure DC focal mechanism and exclude by default the existence non-DC components. However, if this assumption is not valid and the earthquake sources display significant values of CLVD components, the inversion of focal mechanism constrained to DC may produce an apparent rotation in resolved orientation of *P*/*T*/*B* axes. This may be of importance for the stress inversions performed using seismic data where non-DC components are likely to be observed, e.g., fracking operations, mining- or fluid-induced seismicity (cf. discussion on other potential stress rotation mechanisms in *Martínez-Garzón et al.* [2013]).

In summary, our analysis indicated that (a) AE-derived MT characteristics as well as *b* values calculated from FMDs can be used to describe the micromechanical processes occurring stick-slip cycles and reflects the macroscopic deformation occurring in the sample, (b) the observed changes in AE characteristics are clearly correlated to the fault topography and roughness, (c) fault evolution resulting in progressing smoothing of the fault surface can be observed in AE characteristics, (d) the rough surface sample may be a proxy for a very young fault (or a very complex fault zone) with a dominance of compaction and shearing at all AE magnitudes whereas the saw cut surface seem to mimic the mature fault with scarce and small AEs displaying non-DC behavior and large and dominating AEs with shear behavior, and (e) rotations in fault plane parameters can be related to existence of shear-enhanced compaction or extension in the seismic source.

Acknowledgments
We would like to thank G. McLaskey, an anonymous reviewer, and the Editor A.V. Newman for many valuable comments and suggestions. The data used in this study were processed at GFZ German Research Centre for Geosciences and are available on request by contacting the first author.

The Editor thanks Gregory McLaskey and an anonymous reviewer for their assistance in evaluating this paper.

References

Ben-Zion, Y., and J.-P. Ampuero (2009), Seismic radiation from regions sustaining material damage, *Geophys. J. Int.*, *178*(3), 1351–1356, doi:10.1111/j.1365-246X.2009.04285.x.

Ben-Zion, Y., and C. G. Sammis (2003), Characterization of fault zones, *Pure Appl. Geophys.*, *160*(3–4), 677–715, doi:10.1007/PL00012554.

Brace, W. F., and J. D. Byerlee (1966), Stick-slip as a mechanism for earthquakes, *Science*, *153*(3739), 990–992.

Brodsky, E. E., J. J. Gilchrist, A. Sagy, and C. Collettini (2011), Faults smooth gradually as a function of slip, *Earth Planet. Sci. Lett.*, *302*(1–2), 185–193, doi:10.1016/j.epsl.2010.12.010.

Castro, R. R., and Y. Ben-Zion (2013), Potential signatures of damage-related radiation from aftershocks of the 4 April 2010 (Mw 7.2) El Mayor–Cucapah Earthquake, Baja California, México, *Bull. Seismol. Soc. Am.*, *103*(2A), 1130–1140, doi:10.1785/0120120163.

Collins, D. S., W. S. Pettitt, and R. P. Young (2002), High-resolution mechanics of a microearthquake sequence, *Pure Appl. Geophys.*, *159*, 197–219, doi:10.1007/PL00001251.

Davi, R., V. Vavryčuk, E.-M. Charalampidou, and G. Kwiatek (2013), Network sensor calibration for retrieving accurate moment tensors of acoustic emissions, *Int. J. Rock Mech. Min. Sci.*, *62*(0), 59–67, doi:10.1016/j.ijrmms.2013.04.004.

Fischer, T., and A. Guest (2011), Shear and tensile earthquakes caused by fluid injection, *Geophys. Res. Lett.*, *38*, L05307, doi:10.1029/2010GL045447.

Gibowicz, S. J., R. P. Young, S. Talebi, and D. J. Rawlence (1991), Source parameters of seismic events at the Underground Research Laboratory in Manitoba, Canada: Scaling relations for events with moment magnitude smaller than 2, *Bull. Seismol. Soc. Am.*, *81*, 1157–1182.

Goebel, T. H. W., T. W. Becker, D. Schorlemmer, S. Stanchits, C. Sammis, E. Rybacki, and G. Dresen (2012), Identifying fault heterogeneity through mapping spatial anomalies in acoustic emission statistics, *J. Geophys. Res.*, *117*, B03310, doi:10.1029/2011JB008763.

Goebel, T. H. W., C. G. Sammis, T. W. Becker, G. Dresen, and D. Schorlemmer (2013a), A comparison of seismicity characteristics and fault structure in stick-slip experiments and nature, *Pure Appl. Geophys.*, doi:10.1007/s00024-013-0713-7.

Goebel, T. H. W., D. Schorlemmer, T. W. Becker, G. Dresen, and C. G. Sammis (2013b), Acoustic emissions document stress changes over many seismic cycles in stick-slip experiments, *Geophys. Res. Lett.*, *40*, 2049–2054, doi:10.1002/grl.50507.

Goebel, T. H. W., C. Candela, C. G. Sammis, T. W. Becker, and G. Dresen (2014a), Seismic events distributions and off-fault damage during frictional sliding of saw-cut surfaces with predefined roughness, *Geophys. J. Int.*, *196*, 612–625.

Goebel, T. H. W., C. G. Sammis, G. Dresen, and D. Schorlemmer (2014b), Off-fault damage and acoustic emission distributions during the evolution of structurally-complex faults over series of stick-slip events, *Geophys. J. Int.*, *197*, 1705–1718, doi:10.1093/gji/ggu074.

Graham, C. C., S. Stanchits, I. G. Main, and G. Dresen (2010), Comparison of polarity and moment tensor inversion methods for source analysis of acoustic emission data, *Int. J. Rock Mech. Min. Sci.*, *47*(1), 161–169, doi:10.1016/j.ijrmms.2009.05.002.

Knopoff, L., and M. J. Randall (1970), The compensated linear-vector dipole. A possible mechanism for deep earthquakes, *J. Geophys. Res.*, *75*, 1957–1963.

Kwiatek, G., and Y. Ben-Zion (2013), Assessment of P and S wave energy radiated from very small shear-tensile seismic events in a deep South African mine, *J. Geophys. Res. Solid Earth*, *118*, 3630–3641, doi:10.1002/jgrb.50274.

Kwiatek, G., E.-M. Charalampidou, and G. Dresen (2014), An improved method for seismic moment tensor inversion of acoustic emissions through assessment of sensor coupling and sensitivity to incidence angle, *Int. J. Rock Mech. Min. Sci.*, *65*, 153–161, doi:10.1016/j.ijrmms.2013.11.005.

Lockner, D. (1993), The role of acoustic emission in the study of rock fracture, *Int. J. Rock Mech. Min. Sci. Geomech. Abstr.*, *30*(7), 883–899, doi:10.1016/0148-9062(93)90041-B.

Manthei, G. (2005), Characterization of acoustic emission sources in a rock salt specimen under triaxial compression, *Bull. Seismol. Soc. Am.*, *95*, 1674–1700.

Manthei, G., J. Eisenblätter, and T. Dahm (2001), Moment tensor evaluation of acoustic emission sources in salt rock, *Construct. Build Mater.*, *15*(5–6), 297–309, doi:10.1016/S0950-0618(00)00078-7.

Martínez-Garzón, P., M. Bohnhoff, G. Kwiatek, and G. Dresen (2013), Stress tensor changes related to fluid injection at the Geysers Geothermal Field, California, *Geophys. Res. Lett.*, *40*, 2596–2601, doi:10.1002/grl.50438.

McGarr, A. (2012), Relating stick-slip friction experiments to earthquake source parameters, *Geophys. Res. Lett.*, *39*, L05303, doi:10.1029/2011GL050327.

McGarr, A., and J. B. Fletcher (2003), Maximum slip in earthquake fault zones, apparent stress, and stick-slip friction, *Bull. Seismol. Soc. Am.*, *93*, 2355–2362.

McGarr, A., J. B. Fletcher, M. Boettcher, N. Beeler, and J. Boatwright (2010), Laboratory-based maximum slip rates in earthquake rupture zones and radiated energy, *Bull. Seismol. Soc. Am.*, *100*(6), 3250–3260.

McLaskey, G., and S. Glaser (2012), Acoustic Emission Sensor Calibration for Absolute Source Measurements, *J. Nondestruct Eval.*, *31*(2), 157–168, doi:10.1007/s10921-012-0131-2.

McLaskey, G. C., and B. D. Kilgore (2013), Foreshocks during the nucleation of stick-slip instability, *J. Geophys. Res. Solid Earth*, *118*, 2982–2997, doi:10.1002/jgrb.50232.

McLaskey, G. C., and S. D. Glaser (2011), Micromechanics of asperity rupture during laboratory stick slip experiments, *Geophys. Res. Lett.*, *38*, L12302, doi:10.1029/2011GL047507.

Ohtsu, M. (2000), Moment tensor analysis of AE and SiGMA code, in *Acoustic Emission—Beyond the Millennium*, edited by T. Kishi, M. Ohtsu, and S. Yuyama, pp. 19–34, Elsevier, Amsterdam, Netherlands.

Ross, A., G. R. Foulger, and B. R. Julian (1996), Non-double-couple earthquake mechanisms at the Geysers Geothermal Area, California, *Geophys. Res. Lett.*, *23*(8), 877–880, doi:10.1029/96GL00590.

Savage, H. M., and E. E. Brodsky (2011), Collateral damage: Evolution with displacement of fracture distribution and secondary fault strands in fault damage zones, *J. Geophys. Res.*, *116*, B03405, doi:10.1029/2010JB007665.

Sellers, E. J., M. O. Kataka, and L. M. Linzer (2003), Source parameters of acoustic emission events and scaling with mining-induced seismicity, *J. Geophys. Res.*, *108*(B9), 2418, doi:10.1029/2001JB000670.

Stanchits, S., S. Vinciguerra, and G. Dresen (2006), Ultrasonic velocities, acoustic emission characteristics and crack damage of basalt and granite, *Pure Appl. Geophys.*, *163*(5–6), 975–994, doi:10.1007/s00024-006-0059-5.

Stanchits, S., S. Mayr, S. Shapiro, and G. Dresen (2011), Fracturing of porous rock induced by fluid injection, *Tectonophysics*, *503*(1–2), 129–145, doi:10.1016/j.tecto.2010.09.022.

Stierle, E., V. Vavryčuk, J. Šílený, and M. Bohnhoff (2014a), Resolution of non-double-couple components in the seismic moment tensor using regional networks—I: A synthetic case study, *Geophys. J. Int.*, doi:10.1093/gji/ggt502.

Stierle, E., M. Bohnhoff, and V. Vavryčuk (2014b), Resolution of non-double-couple components in the seismic moment tensor using regional networks—II: Application to aftershocks of the 1999 Mw 7.4 Izmit earthquake, *Geophys. J. Int.*, doi:10.1093/gji/ggt503.

Thompson, B. D., R. P. Young, and D. A. Lockner (2009), Premonitory acoustic emissions and stick-slip in natural and smooth-faulted Westerly granite, *J. Geophys. Res.*, *114*, B02205, doi:10.1029/2008JB005753.

Vavryčuk, V. (2001), Inversion for parameters of tensile earthquakes, *J. Geophys. Res.*, *106*(B8), 16,339–16,355, doi:10.1029/2001JB000372.

Wiejacz, P. (1992), Calculation of seismic moment tensor for mine tremors from the Legnica-Glogów Copper Basin, *Acta Geophys. Pol.*, *40*, 103–122.

Zang, A., F. C. Wagner, S. Stanchits, G. Dresen, R. Andresen, and M. A. Haidekker (1998), Source analysis of acoustic emissions in Aue granite cores under symmetric and asymmetric compressive loads, *Geophys. J. Int.*, *135*(3), 1113–1130.